

Quantitative theory of the grain boundary impact on the open-circuit voltage of polycrystalline solar cells

Benoit Gaury^{†,‡} and Paul M. Haney^{*,†}

[†]*Center for Nanoscale Science and Technology, National Institute for Standards and
Technology, Gaithersburg, MD 20899, USA*

[‡]*Maryland NanoCenter, University of Maryland, College Park, MD 20742, USA*

E-mail: paul.haney@nist.gov

Keywords— photovoltaics, grain boundary, thin film, polycrystalline semiconductor,
carrier defect recombination

Abstract

Thin film polycrystalline photovoltaics are a mature, commercially-relevant technology. However, basic questions persist about the role of grain boundaries in the performance of these materials, and the extent to which these defects may limit further progress. In this work, we first extend previous analysis of columnar grain boundaries to develop a model of the recombination current of “tilted” grain boundaries. We then consider systems with multiple, intersecting grain boundaries and numerically determine the parameter space for which our analytical model accurately describes the recombination current. We find that for material parameters relevant for thin film photovoltaics, our model can be applied to compute the open-circuit voltage of materials with networks of inhomogeneous grain boundaries. This model bridges the gap between

the distribution of grain boundary properties observed with nanoscale characterization and their influence on the macroscale device open-circuit voltage.

Polycrystalline materials possess an abundance of extended crystallographic defects in the form of grain boundaries, which are typically harmful to device performance. However, recent development in thin-film photovoltaics have led to surprisingly high efficiencies given the large densities of grain boundaries.¹ The efficiency records were obtained mostly by improvements in light absorption and collection of photogenerated carriers.² Increasing the open-circuit voltage (currently at ≈ 880 mV in polycrystalline CdTe^{2,3}) has proven to be more difficult. Two groups recently reported^{4,5} single crystal CdTe solar cells with open-circuit voltages above 1 V, suggesting that grain boundaries may be an important source of recombination and reduce the open-circuit voltage of polycrystalline solar cells.⁶ While grain boundaries are a predominant source of defects in thin film photovoltaics, a precise understanding of grain boundary recombination and its impact on performance remains uncertain and controversial.⁷ A primary difficulty in experimentally determining the effect of grain boundaries is that modifying grain structure typically changes other important material properties⁷ (as in the studies of Ref. 4,5). Theoretical models are suited to provide guidance in this case, as models afford the freedom to independently vary material and system parameters. The simplest models of grain boundaries⁸⁻¹¹ used for analyzing polycrystalline Si are inconsistent with the high efficiency of thin film photovoltaics, indicating the need for more sophisticated approaches.

On the experimental side, there has been recent substantial progress in characterizing grain boundaries. Nanoscale imaging and spectroscopy can, in some circumstances, reveal the full three-dimensional, chemically resolved atomic structure of grain boundaries.^{12,13} Knowledge of atomic structure enables first principles calculations of the electronic structure of certain ideal grain boundaries, identifying defect energy levels and charge states.¹⁴ Direct measurements of electrical properties of individual grain boundaries using high resolution techniques yield qualitative insights (such as the sign of grain boundary defect charge^{15,16}),

although quantitative interpretation of these measurements remains a challenge. Nevertheless, even perfect knowledge of grain boundary electrical properties would not suffice to determine their impact on important figures of merit, such as the open-circuit voltage. This is due to a gap on the theory side: so far no analytical relation connects grain boundary properties of a realistic sample to its V_{oc} . Here we provide this previously missing component of the theory and demonstrate its validity for material parameters typical of thin film solar cells. While the short circuit current and the fill factor are also key elements of a solar cell efficiency, we focus on the open-circuit voltage as it is the metric for which the largest margin of improvement is available.²

In a series of recent works,^{1,2} we studied the charge transport associated with isolated, columnar grain boundaries in thin film solar cells consisting of n^+p junctions (p -type absorber). We obtained an approximate analytic solution for the grain boundary recombination current under the conditions that the grain boundary is positively charged with large defect density (so that the Fermi level is pinned to the defect neutrality level), and that the majority carrier transport is sufficiently facile so that the quasi-hole Fermi level varies by less than the thermal voltage V_T (≈ 25 meV at room temperature). Under these circumstances, electrostatic screening leads to downward band bending in the vicinity of the grain boundary (shown in Figure 1), which confines electrons near the grain boundary core. We showed that in this case, the two-dimensional problem for the recombination can be mapped to an effective one-dimensional problem for the motion of electrons along the grain boundary. The dark recombination current of an isolated columnar grain boundary versus voltage V is shown to take the following general form²

$$J_{GB}(V) = \lambda \frac{S}{2d} N e^{-E_a/k_B T} e^{qV/(nk_B T)}, \quad (1)$$

where S is an effective surface recombination velocity, λ is the characteristic length over which recombination occurs, d is the grain size, N is an effective density of states, E_a is

an activation energy, n is the ideality factor (k_B is the Boltzmann constant and T is the temperature).

The specific form of the parameters depends on the type (i.e., majority carrier) of the grain boundary core. There are 3 possible cases: 1. n -type, which occurs when the band bending at the grain boundary is large enough to cause type inversion at the grain boundary core (i.e. the Fermi level is closer to the conduction band at the grain boundary core), 2. p -type, where we note that the assumption of downward band bending implies that the grain boundary core will always be less p -type than the bulk of the absorber. For both n -type and p -type grain boundary cases, the majority carriers have a constant concentration along the entire length of the grain boundary. The last case is: 3. Neither n -type or p -type, a case to which we refer as “high recombination”. For this case, there are regions along the grain boundary core at which the electron and hole densities are similar in magnitude, and both carrier densities vary along the length of the grain boundary. The specific expressions of the parameters entering Eq. (1) are given in the Supporting Information and in Ref. 1.

In this work, we focus on microstructures with complex grain boundary topology, as depicted in Figure 2. We first extend our previous model to consider grain boundaries tilted at an angle θ with respect to the pn^+ junction normal. Based on the physical picture of carrier recombination developed in previous works, we make a simple *ansatz* for the dependence of grain boundary recombination on θ . To demonstrate the validity of this *ansatz*, we make comparisons to 2-d numerical simulations performed with the semiconductor modeling software Sesame.³ We next analyze the carrier transport in *networks* of non-columnar grain boundaries. We find that under similar assumptions leading to Eq. (1), the recombination of a particular grain boundary embedded within a network is approximately equal to the recombination of the same grain boundary in isolation. The total dark recombination current of a grain boundary network is therefore given by the sum of its individual contributions, which can be weighted by a statistical distribution of grain boundary parameter values. The description of the orientation-dependence and the network behavior of grain boundary re-

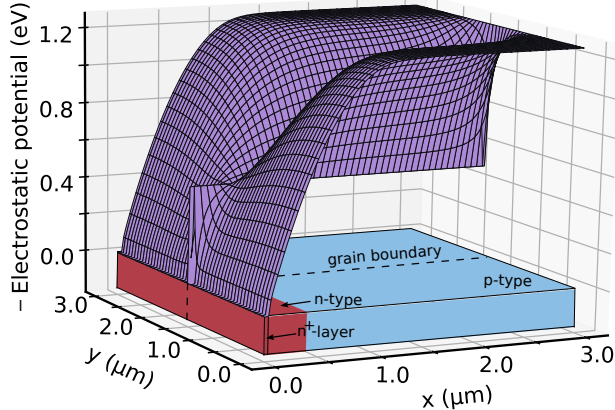


Figure 1: Thermal equilibrium electrostatic potential of a pn^+ junction containing a single charged grain boundary at $y = 1.5 \mu\text{m}$ (dashed line).

combination completes our model. These advances expand the applicability of the model from idealized, artificial geometries to real materials. Our model therefore provides a missing link between nanoscale characterization of the distribution of grain boundary properties and their impact on a real device open-circuit voltage V_{oc} .

We begin with a description of the charge transport of a single grain boundary with one end near the metallurgical pn^+ junction, and oriented an angle $\theta < 90^\circ$, as shown in Figure 3b. We consider grain boundaries which do not make direct connections with the contacts. The physical picture we describe here is based on Ref. 1, which provides more details. Informed by numerical simulations, we first posit that the grain boundary orientation primarily affects the length over which recombination occurs along the grain boundary core. That is, λ of Eq. (1) is assumed to be the only θ -dependent factor. We start with some definitions. W_p is defined as the pn^+ junction depletion width in the grain interior, *i.e.* in a region where the electrostatic potential is unperturbed by the grain boundary (see Figure 3d). x_0 is defined as the position in the grain interior where $n = p$ (in equilibrium), such that $n > p$ for $x < x_0$ (see Figure 3c). The primary quantity of interest is the grain boundary recombination, which occurs at defects located at the grain boundary core. For n -type or p -type grain boundaries, the grain boundary defect recombination is set by the minority carrier concentration, while for high-recombination grain boundaries, both electron

and hole density control the recombination. We summarize the behavior of the system for the three cases below.

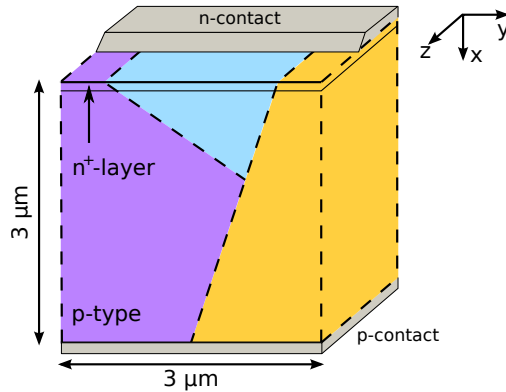


Figure 2: Model system of a pn^+ junction containing several grains and grain boundaries (represented by the dashed lines).

For an n -type grain boundary, recombination is determined by holes. Ref. 1 shows that holes flow from the bulk of the p -type grain interior into the grain boundary core and recombine. The majority of the grain boundary length L_{GB} is embedded in p -type bulk, so holes are available for transport into the grain boundary from the grain bulk over approximately the entire grain boundary length, independent of the orientation θ . The high defect density fixes the quasi-Fermi levels and the electrostatic potential over the entire length of the grain boundary, as shown in Figure 1. Electron and hole densities are therefore uniform along the grain boundary, leading to uniform recombination along the entire grain boundary length L_{GB} . Hence we have $\lambda = L_{GB}$.

The recombination in a p -type grain boundary is determined by electrons, which flow from the n -type grain interior into the grain boundary core. For a perfectly columnar ($\theta = 0^\circ$) grain boundary, the electrons flow into the grain boundary for $x < x_0$, as shown in Figure 3a. The recombination is therefore concentrated within the n -region of the pn^+ junction depletion region, and is uniform for $x < x_0$. As the grain boundary is tilted ($\theta \neq 0^\circ$), a larger section of the grain boundary is exposed to electrons coming from the nearby n -contact, as shown in Figure 3b. This increased exposure expands the region of uniform recombination, which leads to a longer recombination region λ . We find the appropriate form for the increase in

recombination length due to grain boundary tilting is $\lambda = x_0 + W_p \tan(\theta)$, where $W_p \tan(\theta)$ represents the horizontal cross section of the segment of the grain boundary exposed to the electron flow in the depletion region.

Additional recombination occurs as electrons diffuse along the grain boundary, increasing λ . Note that electron transport is not confined to the grain boundary dislocation core (which is of atomic scale), but is spread out over the depletion width surrounding the grain boundary core. We denote the length scale for electron confinement near a grain boundary by $L_{\mathcal{E}}$; for default material parameters (given in Table S2 of the Supporting Information) and moderate grain boundary potentials (e.g 250 eV), $L_{\mathcal{E}}$ is on the order of 0.2 μm . The effective lifetime of confined electrons is then given by $L_{\mathcal{E}}/S$, where S is the effective grain boundary recombination velocity, and their diffusion length L_n is $\sqrt{D_{\text{GB}}^e L_{\mathcal{E}}/S}$, where D_{GB}^e is the diffusivity of the confined electrons (which may be reduced from the bulk value due to disorder at the grain boundary core). For large surface recombination velocities, diffusion lengths of confined electrons are small, and additional recombination away from the pn junction depletion width is negligible. For low surface recombination velocities, diffusion lengths of confined electrons are large and recombination is uniform along the entire grain boundary. The length of the recombination region in these two limits therefore reads

$$\lambda = x_0 + W_p \tan(\theta) \quad \text{for } L_n \ll L_{\text{GB}} \quad (2)$$

$$\lambda = L_{\text{GB}} \quad \text{for } L_n \gg L_{\text{GB}} \quad (3)$$

Equation (2) is valid as long as θ is such that $\lambda < L_{\text{GB}}$; $\lambda = L_{\text{GB}}$ otherwise. Eq. (10) of the Supporting Information gives the general expression for p -type grain boundary recombination for a general value of L_n .

The high-recombination regime of the perfectly columnar grain boundary occurs at sufficiently high applied voltage so that both electron and hole densities are of comparable magnitude. In this case, grain boundary recombination is the result of both electron and

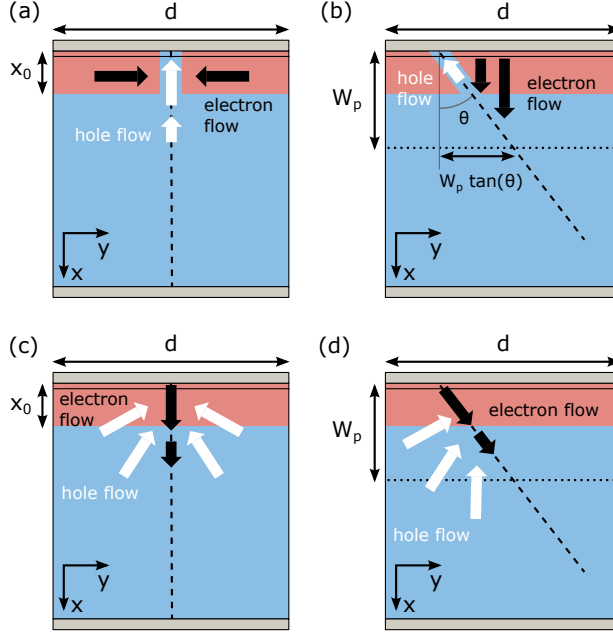


Figure 3: Schematics of the hole and electron particle currents. a), b) In a p -type grain boundary, for $\theta = 0^\circ$ and $\theta > 0$ respectively. c), d) In the high-recombination regime, for $\theta = 0^\circ$ and $\theta > 0$ respectively. W_p is the grain interior depletion region width, x_0 is the point where hole and electron concentrations are equal in the grain interior. Regions in blue and red are respectively p -type and n -type.

hole currents flowing into the grain boundary core. Both carrier types are available only in the vicinity of the depletion region, so that currents flow as depicted in Figure 3c. Holes flow towards the pn^+ junction depletion region to recombine with electrons flowing along the grain boundary core. The recombination is therefore peaked at a “hotspot” in the depletion region.¹ As the grain boundary is tilted, a longer section is exposed to hole flow in the depletion region, as shown in Figure 3d. This larger exposure increases the recombination region length λ in a manner similar to the previous p -type grain boundary case: $\lambda = W_p/2 \tan(\theta)$. Beyond this “hotspot” region, electrons diffuse in a one-dimensional motion along the grain boundary core, as in the p -type grain boundary case described above. We find that the recombination region in the high-recombination regime reads

$$\lambda = \frac{W_p}{2} \tan(\theta) \quad \text{for } L'_n \ll L_{GB} \quad (4)$$

$$\lambda = L_{GB} \quad \text{for } L'_n \gg L_{GB} \quad (5)$$

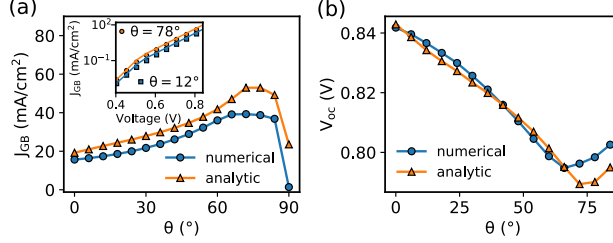


Figure 4: (a) Angular dependence of the current at fixed $V = 0.8$ V. Orange triangles denote analytic result, and blue dots denote numerical result. The grain boundary contains a single donor and acceptor defect at energy $E_{GB} = 0.53$ eV (measured from valence band edge), leading to downward band bending of 0.25 eV, with defect density $\rho_{GB} = 10^{14}$ cm^{-2} , recombination velocity $S_{GB} = 10^5$ cm/s , and length $L_{GB} = 2.8$ μm . Other parameters are given by default values. Inset shows the current-voltage for two different values of θ . Symbols correspond to numerical data, full lines are analytic predictions. (b) The analytical and numerically computed open-circuit voltage as a function of grain boundary orientation (same parameters as in (a)), for an incident photon flux of 2.5×10^{17} $\text{cm}^{-2}\text{s}^{-1}$ and absorption length of 2.3×10^4 cm^{-1} .

where L'_n is the diffusion length of grain boundary-confined electrons in this regime. Equation (4) is valid as long as $\lambda < L_{GB}$, $\lambda = L_{GB}$ beyond that point. Equation (14) of the Supporting Information gives the formula for high-recombination grain boundary current for a general value of L'_n .

To verify the accuracy of the above expressions, we compare our analytical prediction with the results of numerical simulation. Details of the simulation software (along with its source code and a standalone executable) can be found in Ref. 3. The simulation parameters are given in Table S2 of the Supporting Information and in the caption of Fig. 4. Figure 4(a) shows a comparison of the numerically computed grain boundary recombination current (blue dots) and the analytical predictions (orange triangles) as a function of grain boundary orientation for a fixed applied voltage (0.8 V). We find good agreement until the grain boundary becomes nearly completely horizontal, at which point the numerically computed current drops nearly to zero. We find that our model does not describe this full blocking configuration, however it remains accurate at $\theta = 85^\circ$.

We next consider the open-circuit voltage V_{oc} . Our model describes the dark forward bias current, so its applicability to V_{oc} relies on the superposition principle. At high forward bias,

the carrier densities are large enough so that quasi-Fermi levels and the electrostatic potential have negligible differences with those in the dark.²⁰ Because of the high recombination rate of grain boundaries, we find that the current-voltage relation of the pn^+ junction under illumination is given by the sum of the short circuit current J_{sc} and the dark current only near $V = V_{oc}$ (this superposition principle does not apply in our system at lower voltages). We use the analytical model to predict V_{oc} by shifting the analytical dark $J(V)$ curve by the numerically computed J_{sc} . Figure 4(b) shows a comparison between the resulting V_{oc} for analytic and numerical models as a function of grain boundary orientation. In both cases we find good agreement, demonstrating the accuracy of the analytical form for the open-circuit voltage. However we find a large discrepancy for a horizontal grain boundary $\theta = 90^\circ$, where the analytic V_{oc} is less than the numerical value by 0.09 V for the same reasons as the dark current discrepancy given above. We omit this data point in Fig. 4b. The general form of the open-circuit voltage can be found by setting the general form for the high-recombination grain boundary current (given in its full explicit form in Eq. (14) of the Supporting Information) equal to J_{sc} and solving for V .

With a description of the isolated grain boundary recombination current as a function of electrical and geometrical properties, we move on to consider systems with multiple grain boundaries. It is not clear *a priori* that the picture of isolated grain boundary recombination is relevant to an arbitrary configuration of grain boundaries. To address this question, we first reiterate the model conditions and assumptions: 1. Grain boundaries are positively charged. 2. Grain boundaries have “high” defect density (see Supporting Information Eq. (5) for a precise criterion). 3. The hole quasi-Fermi level varies by less than V_T . The validity of assumption 3 is the most difficult to assess. This assumption may fail as a result of poor hole transport, due to low hole mobility and/or low hole carrier concentration. For networks of grain boundaries, the wide variety of possible system geometries and parameters make it difficult to derive a precise and general set of criteria for the validity of assumption 3 and the applicability of the analytical model. In lieu of such a criterion, we numerically explore

parameter space to explicitly find the domain of parameter values for which the analytical model applies.

We consider a system with 3 grain boundaries as depicted in the insets of Fig. 5. The defect energy levels of grain boundary 1, 2, and 3 lead to downward band bending values of (0.71, 0.25, 0.14) eV, respectively (see inset of Fig. 5(c) for grain boundary labels). Fig. (5) provides a comparison of the analytical model with the numerical simulations as a function of hole mobility μ_p and hole doping N_A for three different grain sizes (fixed by system size L_y). We choose these three parameters because they most strongly determine the applicability of the analytical model. We plot the ratio of the analytically predicted to numerically computed dark current at a fixed forward bias voltage $V = 0.8$ V. The red lines delimit the region in parameter space for which the ratio is greater/less than $e \approx 2.7$. We find that dark current ratio values of less than 2.7 correspond to systems for which the analytically predicted V_{oc} deviates from the numerical simulation value by less than the thermal voltage 25 mV (see Fig. S1 of the Supporting Information). As expected, the factors which limit hole transport: low hole mobility and/or low hole carrier concentration due to low hole doping or depleted grains (i.e. grains smaller than the grain boundary depletion width) cause the analytical model to fail. However we find that the analytical model accurately describes the numerical simulation for a wide range of system parameters.

The precise limits of parameter space for which our analytical model applies depends on the details of the grain boundary geometry and defect parameters. For example, if we reduce the electrostatic band bending of grain boundary 1 from 0.71 eV to 0.21 eV, then we find the region of analytic model applicability increases slightly (see Fig. S2 of the Supporting Information). This can be expected: a decreased grain boundary built-in potential decreases the depletion width surrounding the grain boundary, so that hole carriers are less depleted and our assumption of facile hole transport is more easily satisfied. However, we find that the boundaries presented in Fig. 5 give a fairly representative indication of the analytical model's domain of validity. We note that for a grain size of $\approx 1.5 \mu\text{m}$, the analytical

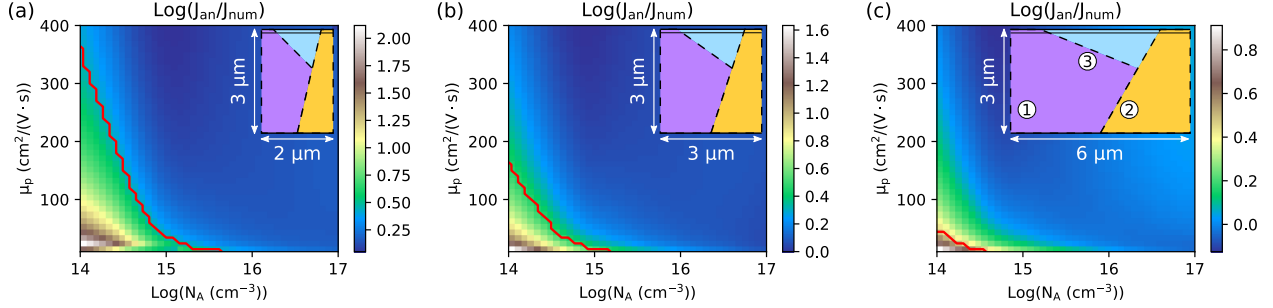


Figure 5: Contour plot of ratio of analytic to numerically computed forward bias dark current at $V = 0.8$ V. Note that color scale is given on a Log_{10} scale. The red line delimits parameter space at which the ratio $J_{\text{an}}/J_{\text{num}} = \exp(1) \approx 2.7$. The electron mobility is fixed to be $8 \times$ the hole mobility. Inset shows schematic of system geometry. Grain boundaries labeled 1, 2, and 3 have built-in potential values of (0.71, 0.25, 0.14) eV and recombination velocities of (10^4 , 5×10^5 , 10^5) cm/s, respectively. Top and bottom edges of schematics represent n and p contacts, respectively. Left and right edges are modeled with periodic boundary conditions. Note grain boundary 1 is located at the left edge.

model can be applied for parameters typical of CdTe absorbers: $\mu_p = 40 \text{ cm}^2/(\text{V} \cdot \text{s})$ and $N_A = 4 \times 10^{14} \text{ cm}^{-3}$.

We consider the behavior of a specific system in more detail in Fig. 6. For this simulation we use default parameter values ($\mu_p = 40 \text{ cm}^2/(\text{V} \cdot \text{s})$, $N_A = 4 \times 10^{14} \text{ cm}^{-3}$). We first show the field lines of the hole currents in Fig. 6a. When the hole currents transverse to both sides of the grain boundary core are equal and opposite (see $x > 2 \mu\text{m}$), the transverse hole current vanishes at the grain boundary core. For $x < 2 \mu\text{m}$, only one side of the grain boundaries has direct access to the p -contact. In this case, hole currents can partially go through grain boundaries, as seen around the left grain boundary. A fraction of the incoming holes recombine at the grain boundary core, so that hole currents on both sides are not equal. Not surprisingly, holes that did not recombine are then attracted preferentially to the grain boundary with the highest surface recombination velocity (“high S” on Figure 6a).

In Figure 6, we plot the numerically computed recombination current of the three grain boundaries separately (symbols), together with the analytical predictions (solid lines). In this case, the analytical theory overestimates the numerically computed current by approximately a factor of 2 at high applied voltage. At low applied voltages, all grain boundaries are

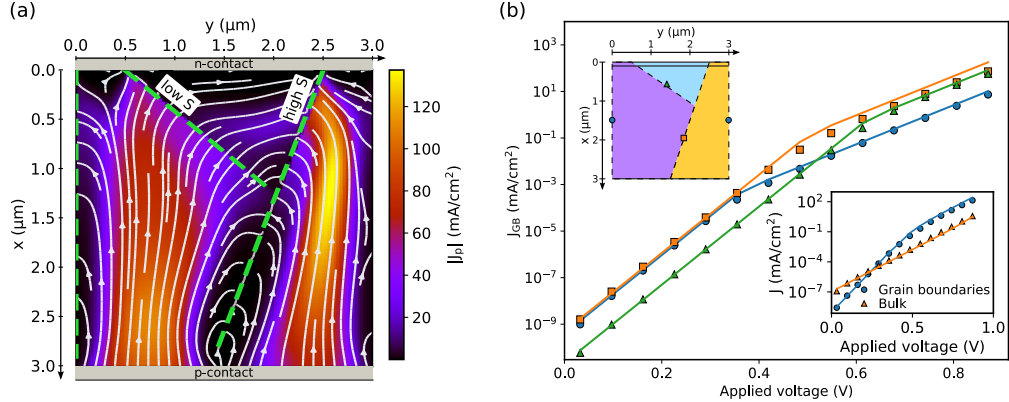


Figure 6: Dark recombination current of a grain boundary network. a) Hole current map for dark current at $V = 0.8$ V. White lines correspond to the hole current field. The effective surface recombination velocity of the grain boundary on the left (“low S ”) is $5\times$ less than the one of the grain boundary on the right (“high S ”). b) Grain boundary dark recombination current as a function of voltage for a structure with multiple grains/grain boundaries as depicted in the upper inset. Symbols are numerical data, full lines are analytic predictions. Grain boundaries characteristics are same as in Fig. 5. Lower inset: sum of the grain boundaries dark recombination currents (blue dots) and bulk recombination current (orange triangles). The analytic predictions for the bulk recombination current is given by Equation (28) and (34) of Ref. 1. Simulation parameters are in Table S2 of the Supporting Information.

either n -type or p -type, with ideality factor of 1. The transition to the high-recombination regime is revealed by the change of slope, corresponding to an ideality factor of 2. The lower inset of Figure 6b compares the total grain boundary and bulk recombination currents (the latter was computed in Ref. 1). In addition to its larger amplitude, the grain boundary’s recombination current exhibits change of slope. For most of the applied voltages, the bulk recombination is proportional to $\exp(qV/(2k_B T))$ as given by the pn^+ junction depletion region recombination.¹ Because of the variety of grain boundary properties in our geometry, the grain boundary most dominating the dark current changes with applied voltage leading to multiple changes of slope between $\exp(qV/k_B T)$ and $\exp(qV/(2k_B T))$. This feature distinguishes grain boundary recombination from pn^+ junction depletion region recombination.

Having established the conditions for which the analytical model describes the behavior of multi-grain boundary systems, we proceed with an analysis of the impact of grain boundary inhomogeneities on the open-circuit voltage using the analytical model alone. We consider

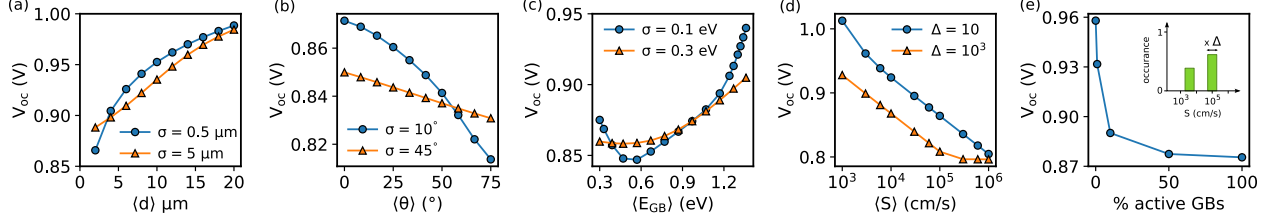


Figure 7: Open-circuit voltage for the system described in Fig. 2 under a photon flux $2.5 \times 10^{17} \text{ cm}^{-2}\text{s}^{-1}$. The absorption coefficient is $2.3 \times 10^4 \text{ cm}^{-1}$. σ is the standard deviation of a Gaussian distribution for a given parameter. $\sqrt{\Delta}$ is the geometric deviation of a uniform distribution. a) V_{oc} as a function of the average grain size d . b) V_{oc} as a function of the average grain boundary angle θ with respect to the normal to the pn^+ junction. c) V_{oc} as a function of the average neutral point of the gap state configuration E_{GB} . d) V_{oc} as a function of the (geometric) average grain boundary effective surface recombination velocity S . e) V_{oc} as a function of the percentage of active grain boundaries for the bimodal distribution shown in inset. Only one parameter is varied on each plot, the others are fixed to: $d = 2.3 \text{ } \mu\text{m}$, $\theta = 0^\circ$, $E_{GB} = 1 \text{ eV}$, $S = 10^5 \text{ cm/s}$.

an ensemble of “samples”, each with its own distributions of grain size, grain boundary orientation, gap state configuration and surface recombination velocity. For a probability distribution P of the random parameter X with mean μ and standard deviation σ , the average grain boundary dark current reads

$$\langle J_{GB}(V) \rangle = \int dX J_{GB}(V, X)P(X; \mu, \sigma) \quad (6)$$

and the open-circuit voltage is found by solving $\langle J_{GB}(V_{oc}) \rangle = J_{sc}$.

Assuming equal short-circuit currents among all “samples”, Figure 7 shows the open-circuit voltage as a function of the mean of the distribution of a grain/grain boundary property. Note that a discussion on the device efficiency, which is beyond the scope of this work, should also include the impact of grain boundary properties on J_{sc} . The integral Equation (6) was computed numerically with the general form for J_{GB} given by Equation (1). We used Gaussian distributions for Figure 7a,b,c, with small (lines with dots) and large (lines with triangles) deviations from the distribution mean. Because surface recombination velocities vary by orders of magnitude, we chose a uniform distribution over the interval $[\langle S \rangle / \sqrt{\Delta}, \sqrt{\Delta} \langle S \rangle]$ for Figure 7d,e, where $\sqrt{\Delta}$ is the geometric deviation of the distribu-

tion. Wide (narrow) distributions represent strong (low) inhomogeneities in the grain/grain boundary property.

V_{oc} varies logarithmically with grain size as shown by the dots in Figure 7a, so only large variations produce significant change in the open-circuit voltage. The weak influence of grain size on open-circuit voltage was observed with photoluminescence measurement on CdTe solar cells.²¹ Figure 7b shows that grain boundaries forming low angles with the normal to the pn^+ junction are always more favorable, almost regardless of the inhomogeneities. The reduction of open-circuit voltage at large angles results from the increase of the length of the recombination region as shown by Equation (4). The gain of approximately 50 mV in V_{oc} (around 5 % increase in typical values of V_{oc} in CdTe) encourages the engineering of a material growth process that increases the proportion of quasi-perfectly columnar grains. Efforts in this direction have been reported.^{22,23}

Figure 7c shows that gap state neutral points E_{GB} close to a band edge generally give better V_{oc} than midgap values. Note that the grain boundary built-in potential attracts photogenerated electrons to the grain boundary core, resulting in enhanced recombination when holes are majority carriers there. The short circuit current is therefore more reduced by p -type than n -type grain boundaries (see Supporting Information), which Figure 7c does not show. Thus, only high values of built-in potential (i.e., $\langle E_{GB} \rangle > 1$ eV) are favorable for the open-circuit voltage. Experimentally, the neutral point of the gap state distribution determines the amplitude of the grain boundary built-in potential V_{GB} . At thermal equilibrium and in the limit of high defect density of states, this relation reads $qV_{GB} \approx E_{GB} - E_F$ (E_F is the bulk Fermi energy). Increasing the spread of E_{GB} results in more gap state neutral levels around midgap. The probability to access midgap states being similar for both electrons and holes, such states provide higher recombination currents than states near the band edge, hence further reducing V_{oc} . These results are consistent with the observation that the standard $CdCl_2$ treatment of CdTe increases the built-in potential around grain boundaries,²⁴ possibly leading to majority carrier type inversion under suitable conditions.^{25,26}

The reduction of the open-circuit voltage by the recombination strength is quantified in Figure 7d,e, where S is the effective surface recombination velocity. We observe the expected logarithmic dependence of V_{oc} on recombination velocity in Figure 7d. The highest surface recombination velocities of the two distributions considered in the figure differ by a factor 10. This is consistent with the difference in V_{oc} of about 50 mV ($\approx k_B T/q \ln(10)$) between the two distributions. This shows that the largest value of surface recombination velocity in the sample determines V_{oc} . Note that because we only allow recombination velocities below the thermal velocity, V_{oc} saturates for $\langle S \rangle > 10^5$ cm/s in the case of $\Delta = 10^3$. The control of the open-circuit voltage by the most deleterious grain boundaries is further illustrated in Figure 7e. A cathodoluminescence study of CdTe grain boundaries revealed that approximately 60 % of the boundaries were active recombination centers.²⁷ Here we show that even a small proportion of active recombination centers is sufficient to degrade V_{oc} . We assumed a bimodal distribution of active and inactive grain boundaries with low ($S_1 = 5 \times 10^3$ cm/s) and high ($S_2 = 10^5$ cm/s) average recombination velocities, as shown in inset. In this instance, we find that a proportion of only 10 % of active grain boundaries gives an open-circuit voltage equivalent to that of a system fully saturated with active grain boundaries. This observation is best understood by assuming that only surface recombination velocities S_1 and S_2 are present in the sample (i.e., a probability distribution with two Dirac delta functions). In this case the average surface recombination velocity across the sample is

$$\langle S \rangle = (1 - p)S_1 + pS_2, \quad (7)$$

where p is the proportion of active grain boundaries. As S_1 and S_2 are separated by orders of magnitude, Equation (7) shows that only a small proportion of active grain boundaries (e.g., $p = 0.1$) is sufficient to dramatically shift the average recombination velocity towards high values.

Our last observation is the resilience of V_{oc} to moderate inhomogeneities, a common feature among the wide parameter distributions. In the high recombination regime (most

relevant around V_{oc}), the dark recombination current varies only algebraically (not exponentially) with all the grain boundary parameters. In turn, the open-circuit voltage varies logarithmically with these parameters, leading to some tolerance towards variations.

In this work, new analytical results were provided for the dark recombination current of grain boundaries forming non-perfectly columnar grains. The model accounts for the main features of grain boundaries: grain size, orientation, gap state configuration and recombination strength. Generalizing the isolated grain boundary picture to networks of grain boundaries is accomplished by finding the parameter space for which contributions of grain boundary recombination can be added independently. We find that for parameters relevant for many thin film photovoltaics, this generalization is valid. Applying these results to random distributions of grain boundary properties led to practical observations regarding the open-circuit voltage. In particular, V_{oc} tolerates moderately heterogeneous grain boundary properties.

To our knowledge, this work is the first fully analytical, quantitative description of grain boundary networks. It contributes to bridge the gap between experimental determination of grain boundary properties and their impact on the device open-circuit voltage. The combination of this theory with nanoscale measurements and first principle calculations can lead to a comprehensive approach to improve the performance of thin-film solar cell technologies.

Supporting information

Explicit form for the analytical current-voltage relations; numerical simulations demonstrating that the analytic dark current-voltage relation accurately predicts the open-circuit voltage; additional numerical simulations demonstrating that the values of grain boundary built-in potential does not appreciably change the regime of validity for the analytical model; table of default simulation parameters

Acknowledgments

B. G. acknowledges support under the Cooperative Research Agreement between the University of Maryland and the National Institute of Standards and Technology Center for Nanoscale Science and Technology, Award 70NANB14H209, through the University of Maryland.

References

- (1) Kumar, S. G.; Rao, K. K. Physics and Chemistry of CdTe/CdS Thin Film Heterojunction Photovoltaic Devices: Fundamental and Critical Aspects. *Energy Environ. Sci.* **2014**, *7*, 45–102.
- (2) Geisthardt, R. M.; Topič, M.; Sites, J. R. Status and Potential of CdTe Solar-Cell Efficiency. *IEEE J. Photovolt.* **2015**, *5*, 1217–1221.
- (3) Gloeckler, M.; Sankin, I.; Zhao, Z. CdTe Solar Cells at the Threshold to 20% Efficiency. *IEEE Journal of Photovoltaics* **2013**, *3*, 1389–1393.
- (4) Zhao, Y.; Boccard, M.; Liu, S.; Becker, J.; Zhao, X.-H.; Campbell, C. M.; Suarez, E.; Lassise, M. B.; Holman, Z.; Zhang, Y.-H. Monocrystalline CdTe Solar Cells With Open-Circuit Voltage Over 1 V and Efficiency of 17 %. *Nat. Energy* **2016**, *1*, 16067.
- (5) Burst, J. M.; Duenow, J. N.; Albin, D. S.; Colegrove, E.; Reese, M. O.; Aguiar, J. A.; Jiang, C.-S.; Patel, M.; Al-Jassim, M. M.; Kuciauskas, D.; Swain, S.; Ablekim, T.; Lynn, K. G.; Metzger, W. K. CdTe Solar Cells With Open-Circuit Voltage Breaking the 1 V Barrier. *Nat. Energy* **2016**, *1*, 16015.
- (6) Sites, J. R.; Granata, J.; Hiltner, J. Losses Due to Polycrystallinity in Thin-Film Solar Cells. *Solar Energy Materials and Solar Cells* **1998**, *55*, 43–50.
- (7) Major, J. D. Grain Boundaries in CdTe Thin Film Solar Cells: a Review. *Semiconductor Science and Technology* **2016**, *31*, 093001.

- (8) Card, H. C.; Yang, E. S. Electronic Processes at Grain Boundaries in Polycrystalline Semiconductors Under Optical Illumination. *IEEE Trans. Electron Devices* **1977**, *24*, 397–402.
- (9) Fossum, J. G.; Lindholm, F. A. Theory of Grain-Boundary and Intragrain Recombination Currents in Polysilicon pn-Junction Solar Cells. *IEEE Trans. Electron Devices* **1980**, *27*, 692–700.
- (10) Green, M. A. Bounds Upon Grain Boundary Effects in Minority Carrier Semiconductor Devices: A Rigorous “Perturbation” Approach With Application to Silicon Solar Cells. *J. Appl. Phys.* **1996**, *80*, 1515–1521.
- (11) Edmiston, S.; Heiser, G.; Sproul, A.; Green, M. Improved Modeling of Grain Boundary Recombination in Bulk and p-n Junction Regions of Polycrystalline Silicon Solar Cells. *J. Appl. Phys.* **1996**, *80*, 6783–6795.
- (12) Wang, Z.; Saito, M.; McKenna, K. P.; Gu, L.; Tsukimoto, S.; Shluger, A. L.; Ikuhara, Y. Atom-Resolved Imaging of Ordered Defect Superstructures at Individual Grain Boundaries. *Nature* **2011**, *479*, 380–383.
- (13) Sun, C.; Paulauskas, T.; Sen, F. G.; Lian, G.; Wang, J.; Buurma, C.; Chan, M. K. Y.; Klie, R. F.; Kim, M. J. Atomic and Electronic Structure of Lomer Dislocations at CdTe Bicrystal Interface. *Sci. Rep.* **2016**, *6*, 27009.
- (14) Yan, Y.; Yin, W.-J.; Wu, Y.; Shi, T.; Paudel, N. R.; Li, C.; Poplawsky, J.; Wang, Z.; Moseley, J.; Guthrey, H.; Moutinho, H.; Pennycook, S. J.; Al-Jassim, M. M. Physics of Grain Boundaries in Polycrystalline Photovoltaic Semiconductors. *J. Appl. Phys.* **2015**, *117*, 112807.
- (15) Yoon, H. P.; Haney, P. M.; Ruzmetov, D.; Xu, H.; Leite, M. S.; Hamadani, B. H.; Talin, A. A.; Zhitenev, N. B. Local Electrical Characterization of Cadmium Telluride

- Solar Cells Using Low-Energy Electron Beam. *Sol. Energ. Mat. Sol. Cells* **2013**, *117*, 499–504.
- (16) Jiang, C.-S.; Noufi, R.; AbuShama, J. A.; Ramanathan, K.; Moutinho, H. R.; Pankow, J.; Al-Jassim, M. M. Local Built-In Potential on Grain Boundary of Cu(In,Ga)Se₂ Thin Films. *Appl. Phys. Lett.* **2004**, *84*, 3477–3479.
- (1) Gaury, B.; Haney, P. M. Charged Grain Boundaries Reduce the Open-Circuit Voltage of Polycrystalline Solar Cells—An Analytical Description. *J. Appl. Phys.* **2016**, *120*, 234503.
- (2) Gaury, B.; Haney, P. M. Charged Grain Boundaries and Carrier Recombination in Polycrystalline Thin-Film Solar Cells. *Physical Review Applied* **2017**, *8*, 054026.
- (3) Gaury, B.; Sun, Y.; Bermel, P.; Haney, P. M. Sesame: a 2-Dimensional Solar Cell Modeling Tool. *arXiv preprint arXiv:1806.06919* **2018**,
- (20) Tarr, N. G.; Pulfrey, D. L. The Superposition Principle for Homojunction Solar Cells. *IEEE Trans. on Electron Devices* **1980**, *27*, 771–776.
- (21) Metzger, W. K.; Albin, D.; Levi, D.; Sheldon, P.; Li, X.; Keyes, B. M.; Ahrenkiel, R. K. Time-Resolved Photoluminescence Studies of CdTe Solar Cells. *J. Appl. Phys.* **2003**, *94*, 3549–3555.
- (22) Luschitz, J.; Siepchen, B.; Schaffner, J.; Lakus-Wollny, K.; Haindl, G.; Klein, A.; Jaegermann, W. CdTe Thin Film Solar Cells: Interrelation of Nucleation, Structure, and Performance. *Thin Solid Films* **2009**, *517*, 2125 – 2131.
- (23) Spalatu, N.; Hiie, J.; Mikli, V.; Krunks, M.; Valdna, V.; Maticiuc, N.; Raadik, T.; Caraman, M. Effect of CdCl₂ Annealing Treatment on Structural and Optoelectronic Properties of Close Spaced Sublimation CdTe/CdS Thin Film Solar Cells vs Deposition Conditions. *Thin Solid Films* **2015**, *582*, 128 – 133.

- (24) Tuteja, M.; Koirala, P.; Palekis, V.; MacLaren, S.; Ferekides, C. S.; Collins, R. W.; Rockett, A. A. Direct Observation of CdCl₂ Treatment Induced Grain Boundary Carrier Depletion in CdTe Solar Cells Using Scanning Probe Microwave Reflectivity Based Capacitance Measurements. *J. Phys. Chem. C* **2016**, *120*, 7020–7024.
- (25) Li, C.; Wu, Y.; Poplawsky, J.; Pennycook, T. J.; Paudel, N.; Yin, W.; Haigh, S. J.; Oxley, M. P.; Lupini, A. R.; Al-Jassim, M.; Pennycook, S. J.; Yan, Y. Grain-Boundary-Enhanced Carrier Collection in CdTe Solar Cells. *Phys. Rev. Lett.* **2014**, *112*, 156103.
- (26) Kranz, L.; Gretener, C.; Perrenoud, J.; Jaeger, D.; Gerstl, S. S. A.; Schmitt, R.; Buecheler, S.; Tiwari, A. N. Tailoring Impurity Distribution in Polycrystalline CdTe Solar Cells for Enhanced Minority Carrier Lifetime. *Advanced Energy Materials* **2014**, *4*, 1301400–n/a, 1301400.
- (27) Moseley, J.; Metzger, W. K.; Moutinho, H. R.; Paudel, N.; Guthrey, H. L.; Yan, Y.; Ahrenkiel, R. K.; Al-Jassim, M. M. Recombination by Grain-Boundary Type in CdTe. *J. Appl. Phys.* **2015**, *118*, 025702.

Supporting information

We use the model for charged grain boundaries of Ref. 1, which is summarized here. A single grain boundary is modeled as a two-dimensional plane with a donor and acceptor gap states at equal energy E_{GB} . This is a convenient model that exhibits Fermi level pinning at a charge neutrality level.⁴ The corresponding grain boundary charge density reads

$$Q_{\text{GB}} = q\rho_{\text{GB}}(1 - 2f_{\text{GB}}), \quad (8)$$

where ρ_{GB} is a two-dimensional defect density. The defect state occupancy is:⁵

$$f_{\text{GB}} = \frac{S_n n_{\text{GB}} + S_p \bar{p}_{\text{GB}}}{S_n(n_{\text{GB}} + \bar{n}_{\text{GB}}) + S_p(p_{\text{GB}} + \bar{p}_{\text{GB}})}, \quad (9)$$

where n_{GB} (p_{GB}) is the grain boundary electron (hole) carrier density, S_n (S_p) is the electron (hole) surface recombination velocity, \bar{n}_{GB} and \bar{p}_{GB} are given by:

$$\bar{n}_{\text{GB}} = N_C e^{(-E_g + E_{\text{GB}})/k_B T} \quad (10)$$

$$\bar{p}_{\text{GB}} = N_V e^{-E_{\text{GB}}/k_B T}, \quad (11)$$

where E_{GB} is a defect energy level calculated from the valence band edge, N_C (N_V) is the conduction (valence) band effective density of states, E_g is the material bandgap, k_B is the Boltzmann constant and T is the temperature. The parameters $S_{n,p}$ and ρ_{GB} are related to the electron and hole capture cross sections $\sigma_{n,p}$ by $S_{n,p} = \sigma_{n,p} v_t \rho_{\text{GB}}$, where v_t is the thermal velocity. In the present work we varied $S_{n,p}$ with fixed ρ_{GB} ; this corresponds to varying $\sigma_{n,p}$ accordingly.

We consider large defect densities of states such that the Fermi level is pinned near the defect energy level E_{GB} (which is the charge neutrality level for this model). This regime was found to be reached for densities above the critical value

$$\rho_{\text{GB}}^{\text{crit}} = \frac{2}{q} \left(\frac{e+1}{e-1} \right) \sqrt{8q\epsilon N_A (E_{\text{GB}} - E_F)} \quad (12)$$

where E_F is the equilibrium Fermi energy and N_A is the doping density. For default material parameters and grain boundary band bending of 0.5 eV, $\rho_{\text{GB}}^{\text{crit}}$ is typically on the order of $5 \times 10^{11} \text{ cm}^{-2}$.

The diffusion length for electrons confined near the grain boundary depends on grain boundary type. We denote this with L_n and L'_n for n -type and high-recombination grain boundary, respectively. The relevant expressions are given below:

$$L_n = 2\sqrt{D_n L_{\mathcal{E}} / S_n}, \quad (13)$$

$$L'_n = \sqrt{8D_n L'_{\mathcal{E}} / \sqrt{S_n S_p}}, \quad (14)$$

where

$$L_{\mathcal{E}} = V_T \sqrt{\frac{2\epsilon}{qN_A V_{\text{GB}}^0}}, \quad (15)$$

$$L'_{\mathcal{E}} = \sqrt{\frac{2\epsilon V_T}{qN_A}}, \quad (16)$$

where $V_T = k_B T / q$. $L'_{\mathcal{E}}$ is the length scale associated with the transverse electric field \mathcal{E}_{\perp} of the grain boundary in the high recombination regime: $L_{\mathcal{E}} = V_T / \mathcal{E}_{\perp}$. In Eq. 15, V_{GB}^0 is the equilibrium potential difference between grain boundary and grain interior.

We next provide the general expressions for the recombination current of p -type and high recombination grain boundaries (the expressions in the main text only show limiting values of L_n / L_{GB} and L'_n / L_{GB} . For p -type, the recombination is given by:

$$J_{\text{GB}}(V) = \frac{S_{\text{GB}} n_{\text{GB}}}{2} \exp\left(\frac{qV}{k_B T}\right) \left[x_0 + W_p \tan \theta + L_n \left(1 - \exp\left(-\frac{L_{\text{GB}} - x_0 - W_p \tan \theta}{L_n}\right) \right) \right] \quad (17)$$

As described in the main text, x_0 is the position where $n = p$ in equilibrium. Its expression

is:

$$x_0 = W_p \left(1 - \sqrt{1 - \frac{V_T}{V_{\text{bi}}} \ln \left(\frac{N_D}{n_i} \right)} \right) \quad (18)$$

where W_p is the bulk depletion width, and V_{bi} is the potential difference of the bulk p - n junction:

$$V_{\text{bi}} = V_T \ln \left(\frac{N_A N_D}{n_i^2} \right) \quad (19)$$

$$W_p = \sqrt{\frac{2\epsilon V_{\text{bi}}}{N_A}} \quad (20)$$

For high-recombination, the recombination is given by:

$$J_{\text{GB}}(V) = \frac{S_{\text{GB}} n_i}{2} \exp \left(\frac{qV}{2k_B T} \right) \left[\frac{W_p \tan \theta}{2} + L'_n \left(1 - \exp \left(-\frac{L_{\text{GB}} - (W_p \tan \theta)/2}{L'_n} \right) \right) \right] \quad (21)$$

We have also checked that grain boundary networks with more complex defect electronic structure, such as a continuum of donors and acceptors (as described in Ref. 2), are accurately described by the approach we present here.

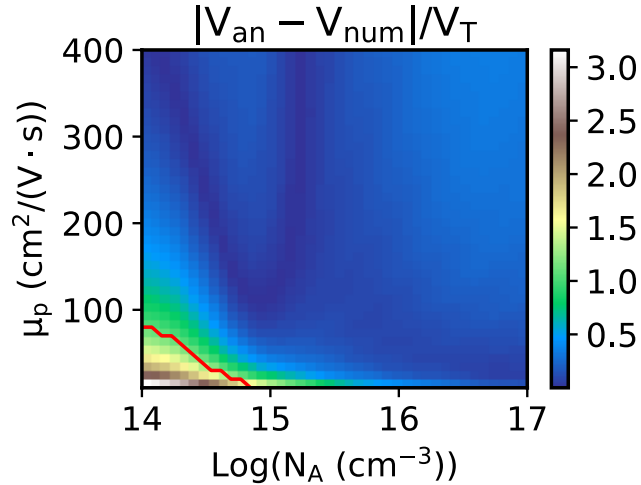


Figure 8: The difference in analytically predicted and numerically computed V_{oc} (scaled by thermal voltage $V_T \approx 25$ mV) for the system given in Fig. 5b of the main text. Red line indicates the parameter values for which this ratio is 1. The electron mobility is fixed to be $8\times$ the hole mobility. Note that the region of the applicability of the analytic model for V_{oc} is similar to the region of applicability for dark $J(V)$ (seen in Fig. 5b).

Figure 8 shows that the reliability of the analytical model’s prediction for V_{oc} tracks its reliability for dark $J(V)$. The red line indicating the region for which the analytical model predicts the numerically computed V_{oc} is similar to the region for which the analytical model predicts the numerically computed dark current to within a factor of $e \approx 2.7$ (see Fig. 5b).

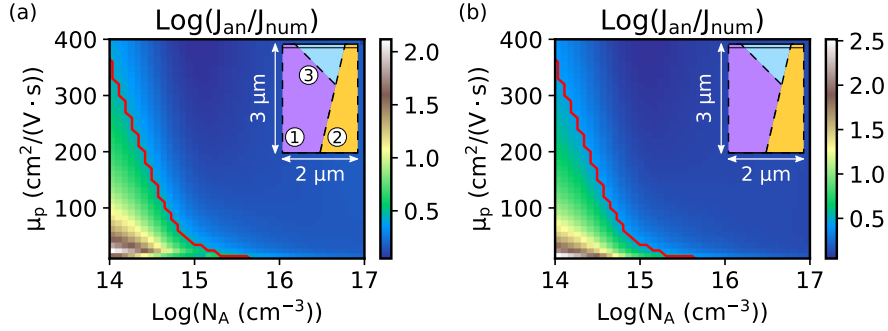


Figure 9: Contour plot of ratio of analytic to numerically computed forward bias dark current at $V = 0.8$ V. Note that color scale is given on a Log_{10} scale. The red line delimits parameters space at which the ratio is $\exp(1) \approx 2.7$ (on a linear scale). Inset shows schematic of system geometry. For (a), grain boundaries labeled 1, 2, and 3 have built-in potential values of (0.71, 0.25, 0.14) V, while for (b) the built-in potential for grain boundary 1 is reduced to 0.21 eV. Recombination velocities for grain boundaries 1, 2, and 3 are $(10^4, 5 \times 10^5, 10^5)$ cm/s, respectively for both (a) and (b). Top and bottom edges of schematics represent n and p contacts, respectively. Left and right edges are modeled with periodic boundary conditions.

Figure 9 shows the dependence of the analytical model performance on the grain boundary built-in potential. We find that this parameter does not strongly influence the model reliability. In general, the smaller the grain boundary built-in potential, the larger the regime of applicability, although the difference is quite small.

We tested our analytical predictions on numerical solutions of the two-dimensional drift-diffusion-Poisson equations, solved using Sesame.³ We used selective contacts, so the hole (electron) current vanishes at $x = 0$ ($x = 3 \mu\text{m}$). Periodic boundary conditions were applied in the y -direction. Table 2 gives a list of the material parameters used in these calculations.

References

- (1) Gaury, B.; Haney, P. M. Charged Grain Boundaries Reduce the Open-Circuit Voltage of Polycrystalline Solar Cells—An Analytical Description. *J. Appl. Phys.* **2016**, *120*, 234503.
- (2) Gaury, B.; Haney, P. M. Charged Grain Boundaries and Carrier Recombination in Polycrystalline Thin-Film Solar Cells. *Physical Review Applied* **2017**, *8*, 054026.
- (3) Gaury, B.; Sun, Y.; Bermel, P.; Haney, P. M. Sesame: a 2-Dimensional Solar Cell Modeling Tool. *arXiv preprint arXiv:1806.06919* **2018**,
- (4) Taretto, K.; Rau, U. Numerical Simulation of Carrier Collection and Recombination at Grain Boundaries in Cu(In,Ga)Se₂ Solar Cells. *J. Appl. Phys.* **2008**, *103*, 094523.
- (5) Shockley, W.; Read, W. T. Statistics of the Recombinations of Holes and Electrons. *Phys. Rev.* **1952**, *87*, 835–842.

Table 1: Summary of analytical results for the grain boundary recombination current for a continuum of donor and acceptor defect states. The general form of the grain boundary dark current is $J_{\text{GB}}(V) = \lambda S / (2d) N e^{-E_a/k_B T} e^{qV/(nk_B T)}$ where S is an effective surface recombination velocity, λ is a length characteristic of the recombination region, d is the grain size, N is an effective density of states, E_a is an activation energy, n is the ideality factor and V is the applied voltage. Each column corresponds to the regime in which the grain boundary is depending on voltage. L_{GB} is the length of the grain boundary, L_n and L'_n are effective electron diffusion lengths.

Param.	n -type	p -type	high-recombination
n	1	1	2
E_a	E_{GB}	$E_g - E_{\text{GB}}$	$E_g/2$
N	N_V	N_C	$\sqrt{N_C N_V}$
S	S_p	S_n	$\sqrt{S_n S_p}$
λ	L_{GB}	L_{GB} for $L_n \gg L_{\text{GB}}$ x_0 for $L_n \ll L_{\text{GB}}$	L_{GB} for $L'_n \gg L_{\text{GB}}$ L'_n for $L'_n \ll L_{\text{GB}}$

Table 2: List of default parameters (Param.) for numerical simulations.

Param.	Value	Param.	Value
L	$3 \mu\text{m}$	ϵ	$9.4 \epsilon_0$
d	$3 \mu\text{m}$	$\tau_{n,p}$	10 ns
N_C	$8 \times 10^{17} \text{ cm}^{-3}$	$S_{n,p}$	$(10^4 \text{ to } 10^6) \text{ cm/s}$
N_V	$1.8 \times 10^{19} \text{ cm}^{-3}$	N_{GB}	10^{14} cm^{-2}
E_g	1.5 eV	(μ_n, μ_p)	$(320, 40) \text{ cm}^2/(\text{V} \cdot \text{s})$
N_D	10^{17} cm^{-3}	N_A	$4 \times 10^{14} \text{ cm}^{-3}$